

Parametrization of the nuclear structure function

G.R.Boroun* and B.Rezaei†

Department of Physics, Razi University, Kermanshah 67149, Iran

(Dated: February 1, 2023)

In this paper, the parametrization of the nuclear structure function which is directly constrained by the dynamics of QCD in its high-energy limit is considered. This simple parameterization of the nuclear structure function is obtained from the proton experimental data by relying on a Froissart-bounded parametrization of the proton structure function. This phenomenological model describes high-energy QCD in the presence of saturation effects. Numerical calculations and comparison with available data from NMC, EMC and E665 Collaborations demonstrate that the suggested method by N.Armento, C.A.Salgado and U.A. Wiedemann (ASW model) provides reliable ratio of nuclear structure functions F_2^A/AF_2^p at low x for light and heavy nuclei. The magnitude of nuclear shadowing is predicted for various kinematic regions and can be applied as well in analysis of ultra-high energy processes by future experiments at electron-ion colliders.

1. INTRODUCTION

The knowledge of the QCD dynamics at high energies is essential in the investigation of hadronic structure studied at current (JLab, RHIC and the LHC) and future with the Electron-Ion Collider (EIC), Large Hadron electron Collider (LHeC), and Future Circular Collider (FCC) accelerators on the horizon. One of the main goals of high energy nuclear physics is to comprehend the sub structure of nucleons in the framework of QCD which is a successful theory in describing the hadronic and nuclear phenomena as well as the inner structure of nucleon and nuclei. In this regard, the structure functions of nucleon and nuclei have played a crucial role. Nuclear structure functions measured in deep inelastic scattering (DIS) experiments (which have been performed by NMC, SLAC, NMC, FNAL, BCDMS, HERMES, and JLAB groups) offer valuable information for understanding the dynamics of partons in the nuclear environment. The correct characterisation of nuclear effects in the parton distribution functions (PDFs) is important due to their relevance in the determination of the proton PDFs and this is baseline for new phenomena in heavy-ion collisions.

Nuclear parton distributions (nPDF) are needed in the computation of inclusive cross sections of hard, factorizable, processes in high energy nuclear collisions. The nuclear effects are generally added as a modification of a baseline PDFs, either by expanding the parametrization or multiplying it by a factor as reported in Refs.[1-12]. There is, in both cases, a dependence on the atomic mass number A . For this reason, there is a continual need for new data sets to broaden global analyses. In this way, groups like EPPS [13], NNPDF [14] or nCTEQ

[15] have been demonstrated the nucleon and nuclear PDF (nPDF) analyses in recent years. Nuclear effects on parton distributions and structure functions are important for interpreting high energy processes involving nuclei such as heavy ions and electron-nucleus collisions at EIC [16] and LHeC/FCC [17]. These colliders (i.e., EIC and LHeC/FCC) are constructive in understanding the momentum distribution of quarks and gluons in nuclei.

At small values of the Bjorken variable x , the non-linear QCD effects will consider in these colliders related to the studies of partonic structure of protons and nuclei [18, 19]. The proposed LHeC collider covers a wide kinematical range down to $x \sim 10^{-6}$ in the perturbative range $Q^2 \gtrsim 1 \text{ GeV}^2$ making it an ideal machine to study small- x physics. In addition to the Large Hadron-electron Collider, the construction of an Electron-Ion Collider with a possibility to operate with a wide variety of nuclei, will allow one to explore the low- x region in much greater detail. In this region a transition between linear and non-linear scale evolution of the parton densities will be crucial [20]. The latter regime, known as "saturation" [21, 22], occurs at low x and low interaction scale Q^2 where the recombination of low x gluons becomes increasingly important.

Also the small x region of QCD can be described theoretically in the effective field theory known as the Color Glass Condensate (CGC); see Ref. [23] for a review. In the CGC picture the non-linear evolution equations describe the evolution of the small x gluon fields. Probing these nonlinearities at the LHeC and EIC are crucial to test the saturation picture [18]. These nonlinearities are important in electron-nucleus scattering in comparison with the electron-proton interactions. The Hadron Electron Ring Accelerator (HERA) did not report the non-linear behavior of the distribution functions in deep inelastic scattering off nuclei at collider energies. Despite this, the future colliders (such as

*Electronic address: grboroun@gmail.com; boroun@razi.ac.ir

†Electronic address: brezaei@razi.ac.ir

LHeC and EIC) will offer unique capabilities to answer the non-linearity in nuclei at high energies [20,24].

The proposed EIC would enable the first direct measurements of nuclear gluons at intermediate and large x using heavy quark probes and could qualitatively advance our understanding of the gluonic structure of nuclei [25]. This collider (i.e., EIC) would have a strong impact, in particular on understanding the small- and large- x regions of nuclear shadowing and the EMC effect in comparison with fixed-target kinematics, which DIS data considerably restricts their range in x and Q^2 , and only with limited statistics for various nuclei [26]. The experiment at EIC is DIS off a proton or a nucleus with the variable center-of-mass energy within the range $20 < \sqrt{s} < 140$ GeV, where this is lower than at HERA with $\sqrt{s} = 318$ GeV, but the luminosity is higher by a factor of 1000. The EIC will combine the experience from HERA to deliver polarized electron beams with the experience from RHIC to be the first machine that provides the collision of polarized electrons with polarized protons, and at a later stage, polarized ^2H and ^3He [27]. At fixed-target facilities, such as JLab, the majority of the momentum is carried by the electron, while for electron-ion collider experiments, the majority of the momentum is carried by the ion beam, so variables are defined according to the electron beam and the ion beam (against the electron beam), respectively. A detailed description of the fixed-target and the EIC 4-momenta is given in [28]. For collider experiments, the center-of-mass energy $\sqrt{s_{\text{EIC}}} = \sqrt{4E_e E_h}$ is often used as a frame of reference and for fixed target experiments the center-of-mass energy $\sqrt{s_{\text{JLab}}} = \sqrt{2m_h E_e + m_h^2}$ where $E_h = m_h$ (target mass). The familiar definitions of Bjorken- x are significantly different between EIC and fixed-target experiments, as for fixed-target experiments $x_{\text{Fixed}} = Q^2/(2m_h\nu)$ where ν is the energy transform $\nu = E_e - E'_e$. In JLab the Bjorken- x scaling is defined $x_{\text{JLab}} = Nx_{\text{Fixed}}$, where N is the number of nucleons in the target. In collider experiments $x = \frac{x_p}{N}$ where $x_p = Q^2/[2E_p(\nu + \nu_z)]$ and $\nu_z = E_e - E'_e \cos\theta_e$. Also the collider definition of W^2 is defined $W^2 = Q^2(1-x)/x$ where in fixed-target experiments it is modified by $W_{\text{JLab}}^2 = m_p^2 + Q^2(1-x_{\text{JLab}})/x_{\text{JLab}}$. Therefore, the kinematic (x, Q^2) range of the fixed-target experiments will be test by EIC as discussed in Ref.[28].

The simplest observable to study nuclear effects is to measure the structure function ratios at small x ($x \leq 0.01$, shadowing region). Indeed, the structure function F_2 per nucleon turns out to be smaller in nuclei than in a free nucleon [24] and this is very important for the study of nuclear structure and nuclear collisions. Nuclear shadowing is a consequence of multiple scattering, as this is well understood in the gluon recombination. Indeed in the frame in which the nucleus is moving fast, the gluon clouds from different nucleons overlap. Therefore the ratio of the structure functions (i.e.,

F_2^A/AF_2^p), at small x , is smaller than 1. The shadowing effect is well understood by the characteristic momentum scale which is known as the saturation scale Q_s^2 . This scale (i.e., saturation scale) increases with decreasing x as $Q_s^2 = Q_0^2(x/x_0)^{-\lambda}$. Geometrical scaling for $\alpha_s(Q^2)xg(x, Q^2)/Q^2$ holds at the boundary $Q^2 = Q_s^2$. For $Q^2 < Q_s^2$ the linear evolution is strongly perturbed by nonlinear effects and for $Q^2 > Q_s^2$ the nonlinear screening effects can be neglected [29].

In this paper a simple parametrization for the nuclear structure function based on the parametrization of the proton structure function is proposed. In Ref.[30] authors have suggested parametrization of the proton structure function which describes fairly well the available experimental data on the reduced cross sections at small x where it is also pertinent in investigations of lepton-hadron processes at ultra-high energies (i.e., the scattering of cosmic neutrinos from hadrons). The parametrization of the proton structure function describes all data on DIS in the region of $x \leq 0.01$ in a wide interval of photon virtualities [30]. Relying on saturation scaling arguments, a simple model for the parameterization of the nuclear structure function is suggested.

2. A MODEL FOR THE NUCLEAR STRUCTURE FUNCTION

It is customary to write the proton structure function F_2 into the cross sections $\sigma_{T,L}$ for the collision of the transversal (T) or longitudinal (L) virtual photon of momentum q , $q^2 = -Q^2$, on the proton as follows

$$F_2^p(x, Q^2) = \frac{Q^2}{4\pi^2\alpha_{em}} [\sigma_T^{\gamma^*p}(x, Q^2) + \sigma_L^{\gamma^*p}(x, Q^2)]. \quad (1)$$

The electron-proton (ep) deep inelastic scattering (DIS) data at small values of the Bjorken variable x can be described within the framework of the dipole model [24,31-35]. In the dipole frame, the incoming photon splits into a $q\bar{q}$ which then interacts with the proton. This process depends on the total dipole-proton cross section, which varies with x and the transverse size r of the dipole. The total γ^*p cross section reads

$$\sigma_{L,T}^{\gamma^*p}(Q^2, Y) = \int d^2\mathbf{r} \int_0^1 dz |\Psi_{L,T}(\mathbf{r}, z; Q^2)|^2 \sigma_{dip}^{\gamma^*p}(r, Y), \quad (2)$$

with $Y = \log(1/x)$ called the rapidity. $\Psi_{L,T}$ is the wave function for the splitting of the virtual photon into a $q\bar{q}$ pair (dipole) and $\sigma_{dip}^{\gamma^*p}(r, Y) = 2\pi R_p^2 N(r, Y)$ is the dipole-proton cross section where N is the dipole-proton scattering amplitude as entering the QCD evolution equations. Here z is a fraction of longitudinal photon momentum carried by quark and R_p is the radius of the proton. The

wave function of the virtual photon, $|\Psi|^2 = |\Psi_T|^2 + |\Psi_L|^2$, in the leading order is given by

$$|\Psi_T(r, z; Q^2)|^2 = \frac{3\alpha_{em}}{2\pi^2} \sum_f e_f^2 \{ [z^2 + (1-z)^2] \bar{Q}_f^2 K_1^2(r\bar{Q}_f) + m_f^2 K_0^2(r\bar{Q}_f) \},$$

$$|\Psi_L(r, z; Q^2)|^2 = \frac{3\alpha_{em}}{2\pi^2} \sum_f e_f^2 4Q^2 z^2 (1-z)^2 K_1^0(r\bar{Q}_f), \quad (3)$$

where $K_{0,1}$ are the Bessel functions, sums \sum_f runs over all quark flavors with charge e_f and mass m_f and also $\bar{Q}_f^2 = z(1-z)Q^2 + m_f^2$.

In the color dipole formalism the nuclear structure function (i.e., F_2^A) is proportional to the dipole nucleus cross section (i.e., $\sigma_{dip}^{\gamma^*A}$). $\sigma_{dip}^{\gamma^*A}$ describes the interaction of the $q\bar{q}$ dipole with the nucleus target. In the eikonal approximation, the total cross-section for dipole to scatter off the target nucleus at an impact parameter \mathbf{b} is given by [1-4,19-35]

$$\sigma_{dip}^{\gamma^*A}(r, Y) = 2 \int d^2\mathbf{b} N_A(\mathbf{r}, Y; \mathbf{b}). \quad (4)$$

The nuclear scattering amplitude $N_A(\mathbf{r}, Y; \mathbf{b})$ depends upon the impact parameter \mathbf{b} , rapidity and dipole size \mathbf{r} . The one dimensionless variable $\tau = Q^2/Q_s^2$ is the geometric scaling where the physics remains unchanged when one moves parallel to the saturation line. Indeed the saturation scale is a border between dense and dilute gluonic systems and the geometric scaling can be understood as a property of the small x evolution equations in the large rapidity regime. In Ref. [36], an analytic interpolation of lepton-proton data as function of the scaling variable $\tau = Q^2/Q_s^2$ was proposed. The ASW form of the single universal curve on σ^{γ^*p} is given by [35]

$$\sigma^{\gamma^*p}(x, Q^2) \equiv \Phi(\tau) = \bar{\sigma}_0 [\gamma_E + \Gamma(0, \xi) + \ln \xi] \quad (5)$$

where γ_E and $\Gamma(0, \xi)$ are the Euler constant and the incomplete Γ function respectively. Authors in Ref.[35] extracted the ξ function from a fit to lepton-proton data as $\xi = a/\tau^b$ with $a = 1.868$ and $b = 0.746$. The normalization is fixed by $\bar{\sigma}_0 = 40.56 \mu b$ and the saturation scale Q_s^2 is parametrized as $Q_s^2 = 1 \text{ GeV}^2 (\bar{x}/x_0)^{-\lambda}$, where $x_0 = 3.04 \times 10^{-4}$, $\lambda = 0.288$ and $\bar{x} = x(Q^2 + 4m_f^2)/Q^2$ with $m_f = 0.14 \text{ GeV}$. The nuclear structure function is defined by $F_2^A(x, Q^2) = Q^2 \sigma^{\gamma^*A}/(4\pi^2\alpha)$ where $\sigma^{\gamma^*A} = \frac{\pi R_A^2}{\pi R_p^2} \sigma^{\gamma^*p}(\tau_A)$ and R_A is the nuclear radius.

In Ref.[33] authors have introduced the saturation scale $Q_s^2(Y) \propto \exp(v_c Y)$ where it is based on an analytic interpolation asymptotic behavior of the amplitude for the unintegrated gluon function. The dipole-proton (nucleus) scattering amplitude is as a result of the Balitsky-Kovchegov (BK) evolution equation [37-38] at high-energy evolution. $Q_s^2(Y)$ is obtained from the knowl-

edge of the Balitsky-Fadin-Kuraev-Lipatov (BFKL) kernel [39] in the form [33]

$$Q_s^2(Y) = k_0^2 \exp(\bar{\alpha} v_c Y), \quad (6)$$

where the parameters of model have been determined according to the HERA data [40] as $v_c = 0.807$, $k_0^2 = 3.917 \times 10^{-3} \text{ GeV}^2$ and $\bar{\alpha} = 3\alpha_s/\pi$. The condition for geometric scaling in the case of $\gamma^* - A$ interactions is defined by the following form [33,35]

$$\sigma_{tot}^{\gamma^*A} \left(\frac{Q^2}{Q_{s,A}^2} \right) = \left(\frac{\pi R_A^2}{\pi R_p^2} \right) \times \sigma_{tot}^{\gamma^*p} \left(\frac{Q^2}{Q_{s,A}^2} \right), \quad (7)$$

where

$$Q_{s,A}^2(Y) = Q_{s,p}^2(Y) \left(\frac{A\pi R_p^2}{\pi R_A^2} \right)^{1/\delta}, \quad (8)$$

and $Q_{s,p}(Y) (\equiv Q_s(Y))$ is the saturation scale for a proton target. In the dipole model, the nuclear data are reproduced for $\delta = 0.79 \pm 0.02$ and $\pi R_p^2 = 1.55 \pm 0.02 \text{ fm}^2$ at low values of x where the nuclear radius is given by the usual parametrization $R_A = (1.12A^{1/3} - 0.86A^{-1/3}) \text{ fm}$ [33,35,41-42]. In the region of small x , the effect of nuclear shadowing manifests itself as an inequality F_2^A/AF_2^p where $\sigma^{\gamma^*A}/A\sigma^{\gamma^*p} \approx F_2^A/AF_2^p$. This leads to the following result for the nuclear structure function

$$F_2^A(\tau_A, Y) = \left(\frac{\pi R_A^2}{\pi R_p^2} \right) \times F_2^p(\tau_A, Y), \quad (9)$$

where the geometric scaling is considered by the following form

$$\tau_A = \tau_p \left(\frac{\pi R_A^2}{A\pi R_p^2} \right)^{1/\delta}, \quad (10)$$

and $\tau_p \equiv \tau = Q^2/Q_s^2(Y)$. The explicit expression for the parametrization of the nuclear structure function F_2^A , is the same of the parametrization of the proton structure function with the change $Q^2 \rightarrow Q_A^2$, where

$$Q_A^2 = \tau \left(\frac{A\pi R_p^2}{\pi R_A^2} \right)^{1/\delta} Q_s^2 = \tau Q_{s,A}^2. \quad (11)$$

In Ref.[30] an analytical expression for the proton structure function, which describes fairly well the available experimental data on the reduced cross section in full accordance with the Froissart predictions, is defined by the following form

$$F_2(x, Q^2) = D(Q^2)(1-x)^n \sum_{m=0}^2 A_m(Q^2) L^m. \quad (12)$$

Therefore the parametrization of the nuclear structure function (according to the Eqs.(9-12)) reads as

$$F_2^A(\tau, Y) = \left(\frac{\pi R_A^2}{\pi R_p^2} \right) D(\tau Q_{s,A}^2) (1 - e^{-Y})^n \times \sum_{m=0}^2 A_m(\tau Q_{s,A}^2) L^m(\tau Q_{s,A}^2, Y), \quad (13)$$

where

$$\begin{aligned} D(Q_j^2) &= \frac{Q_j^2(Q_j^2 + \lambda M^2)}{(Q_j^2 + M^2)^2}, \\ A_0(Q_j^2) &= a_{00} + a_{01} L_2(Q_j^2), \\ A_i(Q_j^2) &= \sum_{k=0}^2 a_{ik} L_2(Q_j^2)^k, \quad i = (1, 2), \\ L(Q_j^2, Y) &= Y + \ln \frac{Q_j^2}{Q_j^2 + \mu^2}, \\ L_2(Q_j^2) &= \ln \frac{Q_j^2 + \mu^2}{\mu^2}, \quad j = p, A. \end{aligned} \quad (14)$$

The effective parameters are defined in Table I.

In the ASW model [35], the nucleon structure function is defined by the following form as

$$F_2^p(\tau) = \frac{Q_{s,p}^2 \tau_p}{4\pi^2 \alpha} [\gamma_E + \Gamma(0, \xi_p) + \ln \xi_p]. \quad (15)$$

The explicit expression for the ratio in this model reads as

$$\frac{F_2^A(\tau_A)}{A F_2^p(\tau)} = \left(\frac{\pi R_A^2}{\pi R_p^2} \frac{Q_{s,A}^2 \tau_A}{A Q_{s,p}^2 \tau_p} \right) \frac{\gamma_E + \Gamma(0, \xi_A) + \ln \xi_A}{\gamma_E + \Gamma(0, \xi) + \ln \xi}, \quad (16)$$

where $\xi_A = a/\tau_A^b$. Notice that Eq.(15) is written in the geometrical scaling whereas the equation (12) is in $(x - Q^2)$ space. Since the cross section in Eq.(7) only depends on Q^2/Q_s^2 , the replacement $Q_{s,p}^2 \rightarrow Q_{s,A}^2$ corresponds to the rescaling $Q^2 \rightarrow Q^2/\lambda_A^2$ in Eq.(12), where $\lambda_A = (\frac{\pi R_A^2}{A \pi R_p^2})^{1/2\delta}$ [43].

3. RESULTS AND CONCLUSIONS

In this section, the numerical calculation of the nuclear structure function and the nuclear ratio using Eqs. (13) and (14) is investigated. With respect to these equations the nucleon and nuclear structure functions and the corresponding ratios for values $x \leq 0.01$ can be computed. Calculations have been performed at a fixed value of the running coupling. For the LO BFKL kernel, one finds $v_c = 0.807$ and $v_c = 4.88\bar{\alpha}$ [33], therefore the coupling constant is fixed by $\alpha_s = 0.17$. The overlap between the models indicates that the Bjorken variable x to

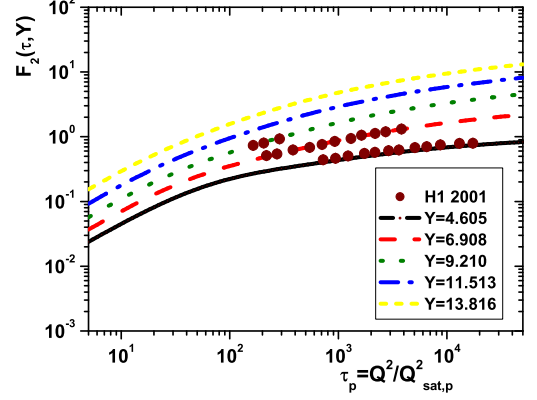


FIG. 1: The proton structure function $F_2(\tau, Y)$ plotted versus scaling variable $\tau_p = Q^2/Q_{\text{sat},p}^2$ for different values of rapidities $Y = \ln \frac{1}{x}$ from $Y_{\text{min}} = 4.605$ (solid curve) to $Y_{\text{max}} = 13.816$ (short-dash curve) compared with the H1 Collaboration data as accompanied with total errors [40], for $x = 10^{-6}, \dots, 10^{-2}$ (curves from up to down, respectively).

vary in the interval $10^{-2} \leq x \leq 10^{-6}$ and Q^2 varies in the interval $0.15 \text{ GeV}^2 \leq Q^2 \leq 150 \text{ GeV}^2$. In Fig.1 the proton structure functions are presented as a function of scaling variable τ for different values of rapidities and compared with the H1 Collaboration data [40]. The proton structure functions obtained into the scaling variable τ are comparable with data of the H1-Collaboration. At intermediate and high scaling variable τ the extracted proton structure functions are in a good agreement with experimental data. The parametrization of the proton structure function is translated to the nuclear structure function as quantified by Eq.(13). To investigate the parametrization model for the nuclear structure function we shall consider results obtained using the scaling variable τ for light and heavy nuclei. In Fig.2 we show the nuclear structure function as a function of scaling variable τ for different values of rapidities and different nuclei. These theoretical curves are the result of the parametrization of the nuclear structure function, meaning that we are using the geometrical scaling in the parametrization method. Furthermore, we check the A -dependence of the nuclear structure function at $Y = 9.210$ in Fig.3. In this figure (i.e., Fig.3), the nuclear structure function decreases as the atomic mass number A increases. It is clear that the A -dependence of the nuclear structure function in electron-nucleus collisions at mid-rapidity involve additional nuclear effects which are at least as significant as nuclear shadowing.

The parameterization method reported by authors in Ref.[35] can be covered all data on photon-nucleon and photon-nuclei, so we compared the nuclear ratio F_2^A/AF_2^p with the experimental data [44] in Fig.5.

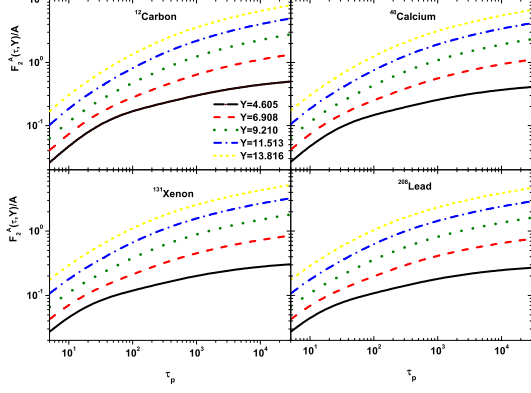


FIG. 2: The nuclear structure function $F_2^A(\tau, Y)$ (normalized to the number of nucleons) plotted versus scaling variable $\tau_p = Q^2/Q_{\text{sat},p}^2$ for different values of rapidities $Y = \ln \frac{1}{x}$, from $Y_{\text{min}} = 4.605$ (solid curve) to $Y_{\text{max}} = 13.816$ (short-dash curve) for Carbon, Calcium, Xenon and Lead nuclei, for $x = 10^{-6}, \dots, 10^{-2}$ (curves from up to down, respectively).

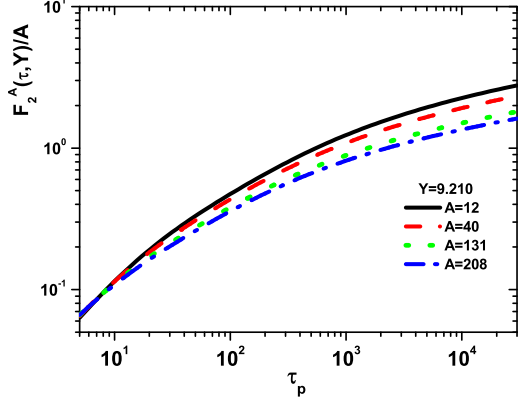


FIG. 3: A -dependence of nuclear structure function (normalized to the number of nucleons) for $A = 12, 40, 131$ and 208 at $Y = 9.210$ ($x = 10^{-4}$) plotted versus scaling variable τ_p .

Figure 5 compares our calculations of the shadowing due to the ASW model (Eq.(16)) with available data from the E665, EMC and EMC Collaborations [44]. The shadowing in nuclei is studied in this figure (i.e., Fig.4) through the ratios of cross sections per nucleon for different nuclei at the Bjorken scaling values $x = 10^{-1}, \dots, 10^{-3}$ respectively. We have selected data where $x < 0.03$ and accompanied with total errors. We observe that for fixed x and large Q^2 , the ratio become closer to one, i.e shadowing decreases with increasing Q^2 and also a larger nuclear shadowing is visible for Lead target at low Q^2 . These results are comparable with others in Refs.[9,42]. In Refs.[9] and [42], nuclear shadowing in the Regge

limit within the Glauber-Gribov model and in the color dipole formalism based on the rigorous Green function techniques at small x have been considered respectively. The behaviors and magnitudes of shadowing using the both color dipole formalism from the higher $|q\bar{q}| > \text{Fock}$ component in Ref.[42] and the parametrization method are comparable. The predictions for expected scaling kinematics in experiments at EICs are presented in Fig.4 for the C, Ca, Xe and Pb targets. Also the ASW model is in good agreement with the dipole model calculation of [45] where rescatterings of the full $q\bar{q} + Ng$ fluctuation is taken into account where the higher Fock-states of the dipole correspond to the summation of triple-pomeron diagrams in that approach. Therefore, these predictions within the parametrization of the nuclear ratios, due to the ASW model, are comparable with other dipole models (such as GBW[46-47], KST[48], BGBK[49], IP-sat[50]).

In conclusion, we studied the shadowing in deep-

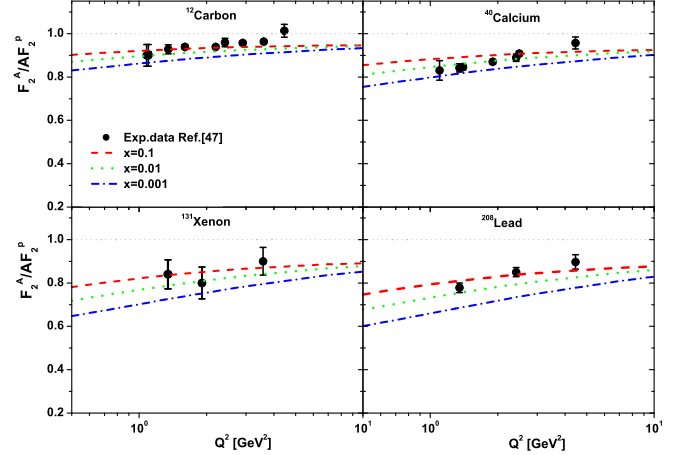


FIG. 4: The nuclear ratio F_2^A/AF_2^p with respect to the ASW model, as a function of Q^2 for several nuclear targets for $x = 10^{-1}, \dots, 10^{-3}$ (curves from up to down, respectively), compared with the experimental data [44] (i.e., E665, EMC and NMC Collaborations) as accompanied with total errors.

inelastic scattering off nuclei in the kinematic regions accessible by the future electron-ion colliders with respect to the parametrization method and the ASW model respectively. We presented a further development of the parametrization of the DIS structure function with respect to the saturation scaling. We calculated the shadowing of the nuclear structure function in the ASW model in the region of $x \leq 0.1$ in a wide interval of photon virtualities. Then we compared the magnitudes of shadowing using the ASW model for the light and heavy nuclei, and showed that that these predictions are in a good agreement with available data from the E665,

EMC and NMC collaborations.

ACKNOWLEDGMENTS

The authors are thankful to the Razi University for financial support of this project. Also G.R.Boroun wishes to especially thank N.Armeστο for reading and commenting on the manuscript.

TABLE I: The effective parameters at low x are defined by the Block-Halzen fit to the HERA data as $M^2 = 0.753 \pm 0.068 \text{ GeV}^2$, $\mu^2 = 2.82 \pm 0.290 \text{ GeV}^2$, $n = 11.49 \pm 0.99$ and $\lambda = 2.430 \pm 0.153$ [30].

parameters	value
a_{10}	$8.205 \times 10^{-4} \pm 4.62 \times 10^{-4}$
a_{11}	$-5.148 \times 10^{-2} \pm 8.19 \times 10^{-3}$
a_{12}	$-4.725 \times 10^{-3} \pm 1.01 \times 10^{-3}$
a_{20}	$2.217 \times 10^{-3} \pm 1.42 \times 10^{-4}$
a_{21}	$1.244 \times 10^{-2} \pm 8.56 \times 10^{-4}$
a_{22}	$5.958 \times 10^{-4} \pm 2.32 \times 10^{-4}$
a_{00}	$2.550 \times 10^{-1} \pm 1.600 \times 10^{-2}$
a_{01}	$1.475 \times 10^{-1} \pm 3.025 \times 10^{-2}$

REFERENCES

1. B.Nachman, K.Wichmann and P.Zurita, arXiv [hep-ph]: 2108.09849.
2. N.Armeστο, H.Paukkunen, C.A.Salgado and K.Tywoniuł, Phys.Lett.B **694**, 38 (2010).
3. K.J.Eskola, H.Honkanen, V.J.Kolhinen and C.A.Salgado, Phys.Lett.B **532**, 222 (2002); arXiv [hep-ph]:0302170.
4. K.J.Eskola, H.Paukkunen and C.A.Salgado, JHEP **0807**, 102 (2008); JHEP **0904**, 065 (2009).
5. S.Kumano and M.Miyama, Phys.Lett.B **378**, 267 (1996); M.Arneodo, Phys.Rept. **240**, 301 (1994); D.F. Geesaman, K.Saito and A.W.Thomas, Ann.Rev.Nucl.Part.Sci. **45**, 337 (1995).
6. E.P.Segarra et al., Phys.Rev.D **103**, 114015 (2021).
7. S.Heidari, B.Rezaei, J.K.Sarma and G.R.Boroun, Nucl.Phys.A **986**, 195 (2019); S.Heidari, B.Rezaei and G.R.Boroun, Int.J.Mod.Phys.E **26**, 1750067 (2017); G.R.Boroun, B.Rezaei and S.Heidari, Int.J.Mod.Phys.A **32**, 1750197 (2017).
8. S.Atashbar Tehrani, Phys.Rev.C **86**, 064301 (2012); J.Sheibani, A.Mirjalili and S.Atashbar Tehrani, Phys.Rev.C **98**, 045211 (2018) ; H.Khanpour, M.Soleymaninia, S.Atashbar Tehrani, H.Spiesberger and V.Guzey, Phys.Rev.D **104**, 034010 (2021).
9. N.Armeστο, A.B.Kaidalov, C.A.Salgado and K.Tywoniuł, Eur.Phys.J.C **68**, 447 (2010).
10. F.Zaidi et al., Phys.Rev.D **99**, 093011 (2019).
11. J.L.Albacete et al., CERN-TH/2003-184, arXiv [hep-ph]:0308050 ; N.Armeστο et al., Eur.Phys.J.C **29**, 531 (2003).
12. S.J.Brodsky, V.E.Lyubovitskij and I.Schmidt, SLAC-PUB-17626, arXiv [hep-ph]:2110.13682.
13. K.J.Eskola, P.Paakkinen, H.Paukkunen and C.A.Salgado, Eur. Phys.J.C **77**, 163 (2017).
14. R.D.Ball et al., Eur.Phys.J.C **77**, 663 (2017).
15. A.Accardi, T.J.Hobbs, X.Jing and P.M.Nadolsky, Eur.Phys.J.C **81**, 603 (2021).
16. A.Accardi, et al., arXiv:1212.1701; D.P.Anderle et al., Front.Phys.**16**, 64701 (2021).
17. LHeC Collaboration and FCC-he Study Group, P. Agostini et al., J. Phys. G: Nucl. Part. Phys. **48**, 110501(2021).
18. Heikki Mäntysaari, arXiv [hep-ph]: 1811.06328.
19. V.P.Goncalves, EPJ Web of Conferences **112**, 02006 (2016).
20. E.C. Aschenauer et al., Phys.Rev.D **96**, 114005 (2017).
21. J.Jalilian-Marian and Y.V.Kovchegov, Prog. Part. Nucl. Phys. **56**, 104 (2006).
22. J. L. Albacete and C. Marquet, Prog. Part. Nucl.Phys. **76**, 1 (2014).
23. F.Gelis, E.Iancu, J.Jalilian-Marian and R. Venugopalan, Annu.Rev.Nucl.Part.Sci.**60**, 463 (2010); L. D. McLerran and R. Venugopalan, Phys.Rev.D **49**, 3352 (1994); E. Iancu, A. Leonidov and L. D. McLerran, Nucl. Phys. A **692**, 583 (2001).
24. N. Armeστο, J.Phys.G **32**, R367 (2006); E.Sichtermann, Nucl.Phys.A **956**, 233 (2016)
25. E. Chudakov et al., Report number: JLAB-THY-16-2329, arXiv [hep-ph]:1608.08686.
26. M.Klasen, K.Kovarik and J.Potthoff, Phys. Rev. D **95**, 094013 (2017).
27. Y.Hatta, Nucl.Phys.A **00**, 1 (2020); O.Bruning, A. Seryi and S. Verdu-Andres, Front.in Phys. **10**, 886473 (2022).
28. E.Long, Technical Note (2019), T19-002.
29. A.Capella et al., Eur.Phys.J.C **5**, 111 (1998).
30. M. M. Block, L. Durand and P. Ha, Phys. Rev.D**89**, 094027 (2014).
31. G. Soyez, arXiv [hep-ph]:0705.3672.
32. C.Marquet, M.R.Moldes and P.Zurita, arXiv [hep-ph]:1702.00839.
- 33.M.A.Betemps and M.V.T.Machado, arXiv [hep-ph]:0906.5593.
34. A.M.Stasto, K.Golec-Biernat, J.Kwiecinski, arXiv [hep-ph]:0007192.
35. N.Armeστο, C.A.Salgado and Urs A.Wiedemann,

- Phys.Rev.Lett. **94**, 022002 (2005).
36. N.Armento, C.Merino, G.Parente, E.Zas, Phys.Rev.D **77**, 013001 (2008).
37. I.I.Balitsky, Nucl.Phys.B **463**, 99 (1996); Phys.Rev.Lett. **81**, 2024 (1998); Phys.Lett.B **518**, 235 (2001).
38. Y.V.Kovchegov, Phys.Rev.D **60**, 034008 (1999); **61**, 074018 (2000).
39. L.N.Lipatov, Sov.J.Nucl. Phys. **23**, 338 (1976); E.A.Kuraev, L.N.Lipatov and V.S.Fadin, Sov. Phys. JETP **45**, 199 (1977); I.I.Balitsky and L.N.Lipatov, Sov.J.Nucl.Phys. **28**, 822 (1978).
40. H1 Collaboration, C.Adloff et al., Eur.Phys.J.C **21**, 33 (2001); ZEUS Collaboration, J.Breitweg et al., Eur.Phys.J.C **12**, 35 (2000); S.Chekanov et al., Eur. Phys. J.C **21**, 443 (2001).
41. J.L.Albacete, N.Armento, J.G.Milhano, C.A.Salgado, U.A.Wiedemann, Eur. Phys. J. C **43**, 353 (2005); Phys. Rev. D **71**, 014003 (2005).
42. M.Krelina and J.Nemchik, Eur.Phys.J.Plus **135**, 444(2020).
43. L.Agozzino, P.Castorina and P.Colangelo, Eur.Phys.J.C **74**, 2828 (2014).
44. M.R.Adams et al. [E665 Collaboration], Phys.Rev.Lett. **68**, 3266 (1992); Z.Phys.C **67**, 403 (1995); M.Arneodo et al. [EMC Collaboration], Nucl.Phys.B **333**, 1 (1990); M.Arneodo et al. [NMC Collaboration], Nucl.Phys.B **441**, 12 (1995); P.Amaudruz et al. [NMC Collaboration], Nucl.Phys.B **441**, 3 (1995).
45. B.Z.Kopeliovich, J.Nemchik, I.K.Potashnikova and I.Schmidt, J.Phys.G **35**, 115010 (2008); B.Z.Kopeliovich, J.Nemchik, N.N. Nikolaev, B.G.Zakharov, Phys.Lett.B **324**, 469(1994).
46. K.J.Golec-Biernat, M.Wusthoff, Phys.Rev.D **59**, 014017 (1998).
47. H.Kowalski, L.Motyka, G.Watt, Phys.Rev.D **74**, 074016 (2006).
48. B.Z.Kopeliovich, A.Schafer, A.V.Tarasov, Phys.Rev.D **62**, 054022 (2000).
49. J.Bartels, K.J.Golec-Biernat, H.Kowalski, Phys.Rev.D **66**, 014001 (2002).
50. A.H.Rezaeian, M.Siddikov, M.Van de Klundert, R. Venugopalan, Phys.Rev.D **87**, 034002 (2013).